International Journal of Plasticity 170 (2023) 103759

Contents lists available at ScienceDirect

International Journal of Plasticity

journal homepage: www.elsevier.com/locate/ijplas

A Hall-Petch-like relationship linking nanoscale heterogeneity to yield stress of heterogeneous metallic glasses

Yucong Gu[a], Jonathan Cappola[a,b], Jian Wang[c], Lin Li[a,b,*]

[a] Department of Metallurgical and Materials Engineering, The University of Alabama, Tuscaloosa, AL 35487, United States
[b] School for Engineering of Matter, Transport and Energy, Arizona State University, Tempe, AZ 85287, United States
[c] Department of Mechanical and Materials Engineering, University of Nebraska-Lincoln, Lincoln, NE 68588, United States

ARTICLE INFO

Keywords:
Metallic glass
Nano-heterogeneity
Shear transformation zone
Shear bands
Hall-Petch-like

ABSTRACT

Metallic glasses (MGs) undergo plastic deformation through shear transformation zones (STZs) at small deformations and shear banding at large deformations. The STZ mechanism is linked to microstructural heterogeneities, including nano-heterogeneities associated with atom clustering and their spatial distribution. Shear banding occurs due to the coalescence of STZs. In this study, we investigate the yielding behavior of heterogeneous MGs by varying the spatial correlation and standard deviation of local shear moduli associated with clustering atoms on the nanoscale. Using a mesoscale shear transformation zone (STZ) dynamics model, we compute the yielding strength and observe deformation behaviors associated with the formation and propagation of STZs. We propose a Hall-Petch-like relationship where the yield stress of the MG scales inversely with the square root of the spatial correlation length. Our results show that the yielding of MGs corresponds to the percolation of STZs from soft to hard regions. Prior to macroscopic yielding, the activated STZs tend to accumulate inside soft regions, forming a Super-STZ array, which is similar to the formation of dislocation pile-up at grain boundaries. We derive the stress concentration in the front of the Super-STZ using the Eshelby inclusion model and formulate a Hall-Petch-like equation to quantify the yield of MGs with the spatial correlation length and standard deviation of the nanoscale heterogeneity. Our results provide insights into the structure-property relationship of MGs and have important implications for the design of nanoscale MGs with tunable properties.

1. Introduction

Metallic glasses (MGs) possess exceptional mechanical properties including high strength and large elastic limit due to their unique structure (Greer et al., 2013; Schuh et al., 2007; Wang et al., 2004). The amorphous structure of MGs, however, is not completely random but exhibits short-range orders (SROs), medium-range orders (MROs), and nanoscale heterogeneity (Hwang et al., 2012; Miracle, 2004; Wakeda and Shibutani, 2010; Wang et al., 2022). Recently, various structural features have been proposed to establish the structure-property relationship that could be correlated with mechanical performance. Atomistic simulations identified a broad spectrum of atomic packing configurations in MGs (Ding et al., 2014a, 2014b). Ding et al. (2021) and Wang et al. (2020) introduced the concept of "soft spots" in MGs, where atoms exhibit quasi-localized soft modes, making them prone to shear transformations. These soft

---

[*] Corresponding author at: School for Engineering of Matter, Transport and Energy, Arizona State University, Tempe, AZ 85287, United States
E-mail address: lin.li.10@asu.edu (L. Li).

https://doi.org/10.1016/j.ijplas.2023.103759
Received 8 June 2023; Received in revised form 3 September 2023;

spots are linked to geometrically unfavored motifs (GUMs), and non-Kasper polyhedra with high disclination density. The spatial distribution of these soft spots in MGs reveals clusters of atoms undergoing shear transformations, indicating a correlation between low-frequency modes and low energy barriers for reconfiguration. Soft spots contribute to low-frequency vibrational modes and are likely to experience atomic rearrangements during deformation. Advanced characterizations have also revealed the presence of nanoscale heterogeneities of structures in MGs (Nomoto et al., 2021; Song et al., 2018a; Tao et al., 2022; Wang et al., 2018a; Yang et al., 2012). For example, Yang et al. (2012) reported the presence of a loose-packing phase in $Zr_{70}Ni_{30}$ samples that exhibit a softer (or liquid-like) nature with an average radius of 2 nm, as resolved using dynamic atomic force microscopy.

The MGs have the salient feature of rich inherent metastable states, and the heterogeneity of the local environment becomes prominent due to the fluctuations. Experimental studies show that the synthesis route and thermomechanical processing can influence the nanoscale heterogeneity and further glass properties (Das et al., 2020; Song et al., 2018a; Zhu et al., 2018; Han et al., 2023). Cryogenic thermal cycling has been used to achieve significant improvement in plasticity in several MGs (Di et al., 2022a, 2020; Du et al., 2020; Song et al., 2018b). The improvement was attributed to the inherent nanoscale heterogeneities and an enlarged soft region population during thermal cycling. Upon sub-T_g annealing, (Zhu et al., 2018) captured the reduction of soft region size in $Zr_{53}Cu_{36}Al_{11}$ MG from hyper-quenched to a relaxed glass state, which was accompanied by a transition of deformation behavior from homogenous plastic flow to shear banding. Even though the transition in deformation mode is often attributed to the evolution of nanoscale structural heterogeneities and soft regions, the relationship between structure, particularly the size and spatial distribution of soft regions, and mechanical properties, remains largely elusive.

The impact of nanoscale heterogeneity on the mechanical properties of MGs is related to the deformation mechanisms underlying MG plasticity and the shear banding process, significant progress has been made in understanding the detailed deformation mechanisms in the past decade (Greer et al., 2013; Gu et al., 2022; Liu et al., 2011; Ma and Ding, 2016; Yang et al., 2012; Zhang et al., 2022a; Zhao et al., 2021, 2017). It is generally accepted that MG deformation involves the activation of shear transformation zones (STZs) in response to thermomechanical stimuli. The STZs are prone to form in loosely packed regions of large free volume (Di et al., 2022b; Jiang et al., 2011), high entropy (Gong et al., 2020; Zhou et al., 2019), or geometrically unfavored structures (An et al., 2016; Şopu et al., 2017). The STZs interact through an Eshelby-like quadrupolar stress field, and when the number of STZs reaches a threshold, the spatial and temporal correlation of local plastic events evolves into the formation of shear bands (Bian et al., 2020; Maloney and Lemaitre, 2006). The formation and propagation of shear bands allow for strain accommodation and energy dissipation, playing a crucial role in the plastic deformation of MGs (Jiang et al., 2008; Tao et al., 2022; Yuan and Branicio, 2020). Recently, an STZ-vortex autocatalyzing mechanism for heterogeneous nucleation and spread of shear bands has been proposed in model MGs using molecular dynamics simulations (Şopu et al., 2020b, 2017). Despite the physical insights, the deformation processes resolved by the atomistic model could be significantly influenced by the hypothetical MG samples prepared by the exceedingly high cooling rates (Zhang et al., 2022b). Additionally, theoretical frameworks based on hierarchically correlated atomic theory are developed to quantitatively describe non-elastic deformation in MGs, validated through stress relaxation and creep experiments, offering insights into the non-elastic deformation mechanisms (Hao et al., 2022). Meso-scale modeling efforts have also been used to elucidate the process of STZs into shear bands under various thermomechanical loadings (Zhao et al., 2013, 2014) and even in the presence of structural fluctuation (Şopu et al., 2020a; Zhu et al., 2018). Wang et al. (2018b) found a critical characteristic length of the nanoscale heterogeneity gave rise to homogenous plastic flow, which was associated with a transition of the shear banding mechanisms from stress-dictated nucleation/growth to structure-dictated strain percolation. Gu et al. (2022) reported a transition in strain rate sensitivity of the heterogeneous thin film MGs due to the dynamical competition between structure- and stress-induced strain localization. Nevertheless, the mechanistic understanding is still missing the connection between nanoscale heterogeneity, microscopic shear banding behavior, and plasticity in heterogeneous MGs.

In this study, we investigate the influence of nanoscale heterogeneity on the plasticity of MGs, with a particular focus on yielding and shear banding behaviors. We utilize a mesoscale STZ dynamics model to simulate the heterogenous MGs by tuning the spatial correlation and standard deviation of local shear moduli on the nanoscale. Interestingly, we observe a Hall-Petch-like relationship between the yield stress and the spatial correlation length of elastic fluctuations. We further delve into details by resolving the spatiotemporal correlation of STZs as they evolve shear bands and interact with structural heterogeneity. The percolation of STZs from soft to hard regions gives rise to the critical moment for the macroscopic yielding. Prior to yielding, the STZs activate and accumulate inside soft regions and form a Super-STZ. We propose a Super-STZ model to describe the stress concentration in front of the Super-STZ. Finally, we formulate a Hall-Petch-like equation to quantify the yield of MGs with the nanoscale heterogeneity.

2. Methodology

2.1. Mesoscale shear transformation zone (STZ) dynamics model

A mesoscale STZ dynamics model that integrates the kinetic Monte Carlo (kMC) and the finite element method (FEM) is adopted to resolve the spatiotemporal correlation of STZs. The STZs are localized clusters of atoms that respond to external stimuli by undergoing characteristic shear transformation (Bulatov and Argon, 1994; Homer et al., 2010; Homer and Schuh, 2009). Using a coarse-graining technique, the STZ dynamics model represents the cluster of atoms that undergoes inelastic rearrangement with a group of elements on a finite element mesh. Thereby, the coarse-grained STZ shearing in a similar manner to the cluster of atoms enables the model to efficiently simulate large systems. In addition, the transition state theory is employed to calculate the rate of the unsheared-to-sheared transition of STZ (Homer et al., 2010). The stochastic activations of STZs are modeled as a Markov process controlled by the kMC algorithm, enabling the model to explore a longer timescale efficiently.

Specifically, at each time step of the STZ dynamics simulation, the activation rate of each potential STZ along one shear direction is calculated as

$$\dot{s}_{STZ} = \nu_{STZ}\exp\left(-\frac{\Delta F(\mu) - \tau\Omega_0\gamma_0/2}{k_B T}\right) \tag{1}$$

where ν_{STZ} is the attempt frequency $\sim 1.02 \times 10^{12}$/s (Homer and Schuh, 2009), which is approximately equal to the Debye frequency and estimated using the Debye temperature of MG. Ω_0 is the activation volume of the STZ, estimated to be 2.7 nm^3 based on literature (Callister, 2000; Pan et al., 2008). γ_0 is a characteristic shear strain increment that occurs during STZ transition and is set to 0.1 according to Argon's model (Argon, 1979; Zink et al., 2006). τ is local shear stress and k_BT represents the thermal energy. ΔF is the activation energy barrier of a potential STZ and is taken as a linear function of the local shear modulus μ (Wang et al., 2018b). The parameters and their values used in the STZ dynamics simulation are summarized in Table 1.

In each step, the kMC algorithm (Homer and Schuh, 2009) is employed to select an STZ that undergoes the characteristic shear transformation γ_0 and determine the elapsed time based on the accumulated activation rate of each STZ in the sample. During each time step, the kMC generates two random numbers, λ_1 and λ_2, uniformly distributed on the interval (0, 1]. A single potential STZ is chosen from the entire model domain and activated. To do so, the activation rate $\dot{s}_i$ for each i-th STZ is calculated according to Eq. (1). The probability, η_i, that a given STZ will be chosen is proportional to its calculated activation rate at the current time step, with the probability for all STZs being normalized by the cumulative activation rate, $\dot{s}_T$, for all STZs,

$$\eta_i = \dot{s}_i/\dot{s}_T \tag{2}$$

where $\sum_i \eta_i = 1$. The random number, λ_1, is used to select an STZ and determine the shear direction of the selected STZ. After an STZ is selected, the elapsed system time is calculated by $\Delta t = -\ln\ \lambda_2/\dot{s}_T$ and the FEM is used to solve the stress and strain redistribution as a result of the selected STZ activation. As the simulation proceeds, the activated STZs interact with each other via the elastic field, leading to deformation behaviors at a large scale. The macroscopic loading/deformation is applied to the MG through FEM boundary conditions, and the simulated MG accommodates the macroscopic loading/deformation via stochastic activations of STZs.

In this study, 2D MG samples have dimensions with a length of 300 nm and a width of 100 nm. Plane-strain quadratic triangular elements (CPE6MT) are used in this study. Each STZ comprises 13 elements, the mesh density of which balances the solution accuracy and computational efficiency (Homer and Schuh, 2009). Tensile loading is along the length direction. The sides of the MG sample parallel to the tensile direction are unconstrained, while the top and bottom surfaces are free to move horizontally with respect to each other. The tensile test is performed under displacement control at 300K, where the bottom nodes are fixed, and the top nodes are moved at a constant strain rate of 0.01/s.

2.2. MGs with various degrees of nanoscale heterogeneity

We prepare MG samples with various degrees of nanoscale heterogeneity by tuning the spatial correlation length ξ and standard deviation δ of the local shear moduli of each element, as shown in Fig. 1. Notably, we adopt a Gaussian distribution for the local shear moduli, a selection supported by its alignment with atomistic simulations (Cheng and Ma, 2009; Fan et al., 2014), and the energy dissipation characteristics resolved through atomic force microscopy (Liu et al., 2011; Zhu et al., 2018).

The construction of a heterogenous MG begins by discretizing the 2D space with uniform grid points, establishing the domain for subsequent calculations. Specifically, a grid of points is then generated forming a 100 by 300 matrix, allowing for spatial analysis. A covariance matrix that captures the transformation of pairwise distances into covariance values is then calculated as

$$\beta_{i,j} = \exp\left(-\varphi\ r_{i,j}\right) \tag{3}$$

where $\beta_{i,j}$ represents the covariance between elements i and j, while φ controls the rate of decay and $r_{i,j}$ is the distance between these elements. φ is the parameter that controls the correlation length ξ, $\varphi = -\alpha/\xi$, where α is a fitting parameter between 1 and 3 (Chiles and Delfiner, 2012).

Table 1
List of simulation parameters used in STZ dynamics simulations.

Simulation parameters	Value
STZ activation volume, Ω_0 Zink et al. (2006)	2.7 nm^3
STZ shear strain, γ_0 Homer et al. (2010)	0.1
Average shear modulus, $\overline{\mu}$	31 GPa
Spatial correlation length, ξ	0.5, 3, 4, 5, 6, 7, 9, and 11 nm
The standard deviation of local shear moduli distribution, δ	2.2 – 5.5 GPa
STZ activation energy, $\Delta F(\mu)$	9.1×10^{-30} J $\times$ Pa^{-1} $\times \mu$
Poisson's ratio, ν	0.36
Temperature, T	300 K
Tensile strain rate	0.01/s
Model dimensions	100 nm × 300 nm

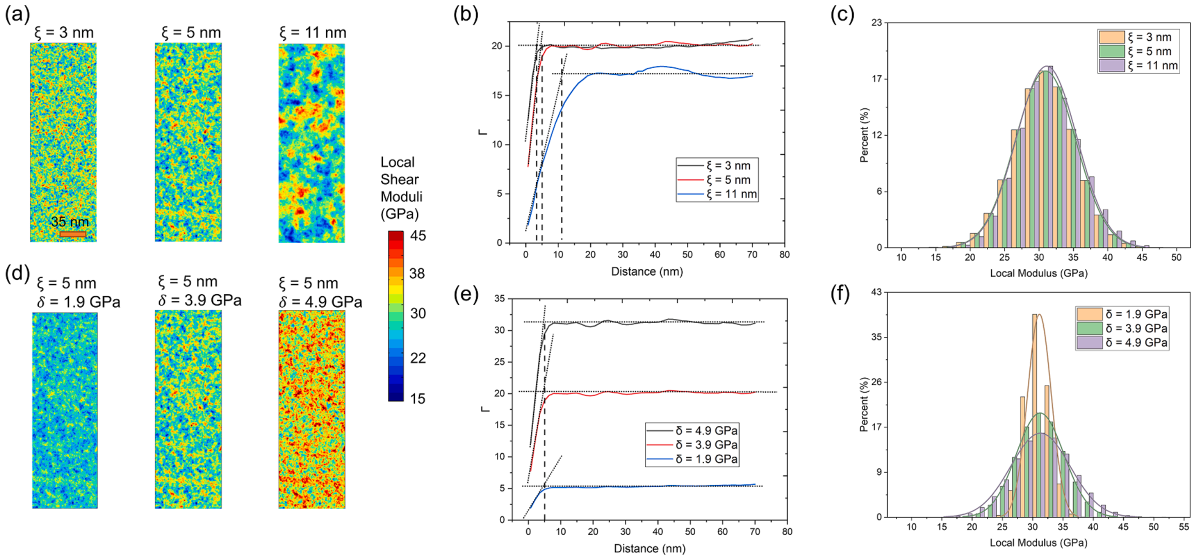

Fig. 1. Examples of the simulated MGs. The heterogenous MG samples with various spatial correlation lengths of local shear moduli in (a)–(c), and with various standard deviations in (d)-(f). The different degrees of heterogeneities are illustrated in the spatial distributions in (a, b), autocorrelation function (b,e), and statistical distributions (c,f) of local shear moduli.

After the covariance matrix is calculated, a multivariate normal distribution using the mean vector ϑ and the covariance matrix β, effectively obtaining a set of 30,000 data points that meets the correlation length requirements. The probability density function of the 2D multivariate normal distribution used is:

$$f(x,\vartheta,\beta) = \frac{1}{\sqrt{|\beta|(2\pi)^2}}\exp\left(-\frac{1}{2}(x-\vartheta)\beta^{-1}(x-\vartheta)'\right) \tag{4}$$

where x is a 2D random vector. ϑ is a vector of length 30,000, i.e., the number of grid points in the MG domain, and all elements are set to have the value of the average shear modulus of the MG.

The generated sample with a modulus set μ_{old} is then rescaled to have the desired standard deviation, generating the final samples, as follows:

$$\mu_{new} = \mu_{mean} + (\mu_{old} - \mu_{mean})\frac{\delta_{old}}{\delta_{new}} \tag{5}$$

where μ_{mean} is the mean of shear moduli, and δ_{old} is the original standard deviation of the modulus distribution from Eq. (4).

The spatial variability of local shear moduli at different lag distances can be visualized by using semi-variogram plots, as shown in Fig. 1(b) and (e). The y-axis displays values of semi-variance Γ, reflecting the extent of difference between shear moduli values at the locations that have a lag distance r. At a small lag distance r, the shear moduli are strongly correlated with little variance and thus a small value of Γ. As the lag distance r increases, the shear moduli are no longer correlated, and the semi-variance Γ becomes constant, equivalent to the square of the standard deviation. Those plots are plotted using the spatial autocorrelation function Γ as follows (Kalogirou, 2016):

$$\Gamma(\mathrm{r}) = \frac{1}{2N(r)}\sum_{N(r)}\left(\mu_{r_0+r} - \mu_{r_0}\right)^2 \tag{6}$$

where $N(r)$ is the number of pairs with a spatial distance equal to r, with r denoting the magnitude of the distance. Γ measures the degree of similarity of properties of any two points with r distance apart. The range, identified as ξ, is the distance beyond which local shear moduli in a sample are no longer auto-correlated, as evidenced by an insignificantly increasing Γ with distance. From the plot, such as Fig. 1(b), the point where semivariance is leveled off can be attained, and the distance at this point is identified as the correlation length ξ of a given case.

Fig. 1(a–c) illustrates a group of heterogenous MG samples with a similar standard deviation of local shear modulus distribution but different spatial correlation lengths ξ. The enhanced spatial correlation leads to the formation of large regions over which the properties are strongly correlated, resulting in a noticeable growth of soft and hard region size. Secondly, the standard deviation of the local moduli δ is another factor controlling the MG heterogeneity. Fig. 1(e,f) shows a group of samples with the same spatial correlation length but different standard deviation δ. The increase in δ strongly enhances the elastic contract between the soft and hard regions but leaves their spatial pattern unchanged.

Here, we use $Cu_{50}Zr_{50}$ as a model system to calibrate the range of material parameters. Based on the experimental results (Xu et al., 2004), we set the local shear moduli to 31 GPa and the Poisson's ratio to 0.36. The standard deviation of local shear moduli varies from 3.2 to 5.5 GPa, which was informed by atomistic simulations (Cheng and Ma, 2009; Duan et al., 2006; Fan et al., 2014; Mayr, 2009). The spatial correlation lengths are tuned between 0.5 to 11 nm being consistent with the range of experimental measurements (Ke et al., 2014; Liu et al., 2011; Mayr, 2009; Ross et al., 2017; Zhu et al., 2018). Notably, the local elastic fluctuation also affects the propensity to undergo the shear transformation, as the STZ activation barrier is proportional to the local shear modulus. Using these methods and parameters, we generate a set of 2D samples with the dimensions of 100 nm by 300 nm. Six randomly designed samples are created under the same parameters to account for the variation in the stress-strain response and shear banding behavior. This allows us to estimate the uncertainty associated with the results. All generated samples are then mapped to a finite element mesh consisting of 173,740 elements for simulations.

3. Results

3.1. Microstructural feature of soft regions with respect to the correlation length

To analyze the microstructural features, a binary classification approach is employed to categorize model MGs into hard or soft regions (Ding et al., 2014a, 2014b), similar to the study done by Şopu et al. (2020b). In order to quantify the relationship between mechanical properties and nanoscale heterogeneity of MGs, we focus on the elastically soft regions because of a significant shear transformation propensity when compared to the hard regions. A soft region here is defined as a cluster of mesh elements with local shear moduli lower than the average shear modulus of the MG and with a region size larger than an STZ (i.e., 2.7 nm^3). Additionally, "soft" mesh elements must not only share edges but also possess connectivity with surrounding "soft" mesh elements.

Following this definition, Fig. 2(a) shows the variation of the average modulus and the average radius of all the soft regions with the

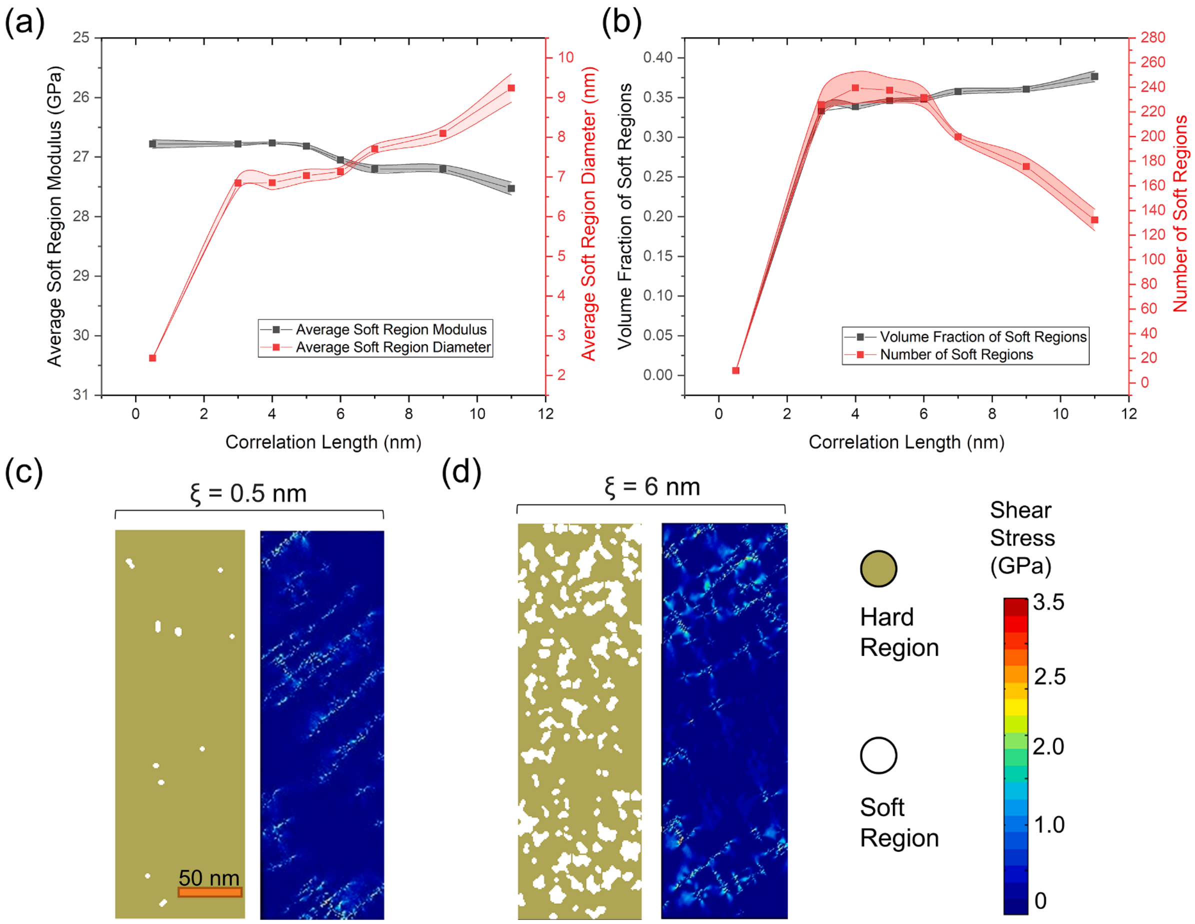

Fig. 2. The spatial correlation lengths of nanoscale heterogeneity vs characteristics of the soft regions. (a) The average modulus and diameter of the soft regions as a function of the correlation length. (b) The volume fraction and the number of soft regions as a function of the correlation length. (c-d) The soft regions and the corresponding local shear stress maps prior to yielding for the simulated samples with $\xi = 0.5$ nm and $\xi = 6$ nm, respectively.

correlation length ξ. It is noted that the average modulus remains roughly constant (~26 GPa), while the average diameter increases with an increase in the correlation length ξ. Fig. 2(b) shows that the volume fraction of soft regions increases with the increase of ξ, but for the larger ξ the volume faction change remains very small. Correspondingly, the number of soft regions peaks around 4 nm. Fig. 2(c, d) shows the distribution of soft regions in two samples with $\xi = 0.5$ nm and $\xi = 6$ nm, respectively. There is a near absence of soft regions (~10) in the $\xi = 0.5$ nm sample, while there is a high abundance (~230) in the $\xi = 6$ nm sample. This significant difference in the number of soft regions can result in a vast difference in the shear response at yielding. For the case of $\xi = 0.5$ nm, the absence of soft regions reduces the likelihood of shear band nucleation at any specific sites. The distribution of shear stress exhibits a more concentrated linear pattern, with small regions at significantly higher stress levels than the rest of the domain. Since nucleation of STZs is dictated by stress, once it occurs, STZs grow rapidly into a dominant shear band. In contrast, local shear stress diffuses across all soft regions in the $\xi = 6$ nm case, which increases the likelihood of shear band nucleation in any soft regions, resulting in a lack of predominant shear bands. It is noteworthy that there is a rough proportionality between the radius of soft regions and the correlation length. As the radius increases, the likelihood of shear band nucleation in these regions also increases. In addition, an increasing number of soft spots results in a more uniformly distributed distribution of soft regions throughout the sample, potentially giving rise to a more homogenous plastic flow.

3.2. Microstructural feature of soft regions with respect to the standard deviation

Fig. 3(a) shows the variation of the average shear modulus and the average radius of all the soft regions with the standard deviation δ. The average shear modulus monotonically decreases as the standard deviation increases, whereas the corresponding average diameter slightly increases. Fig. 3(b) shows a similar increasing trend for both the volume fraction and the number of soft regions as δ increases. Fig. 3(c,d) illustrates the impact of standard deviation on the soft region statistics. The soft region characteristics in the $\delta =$

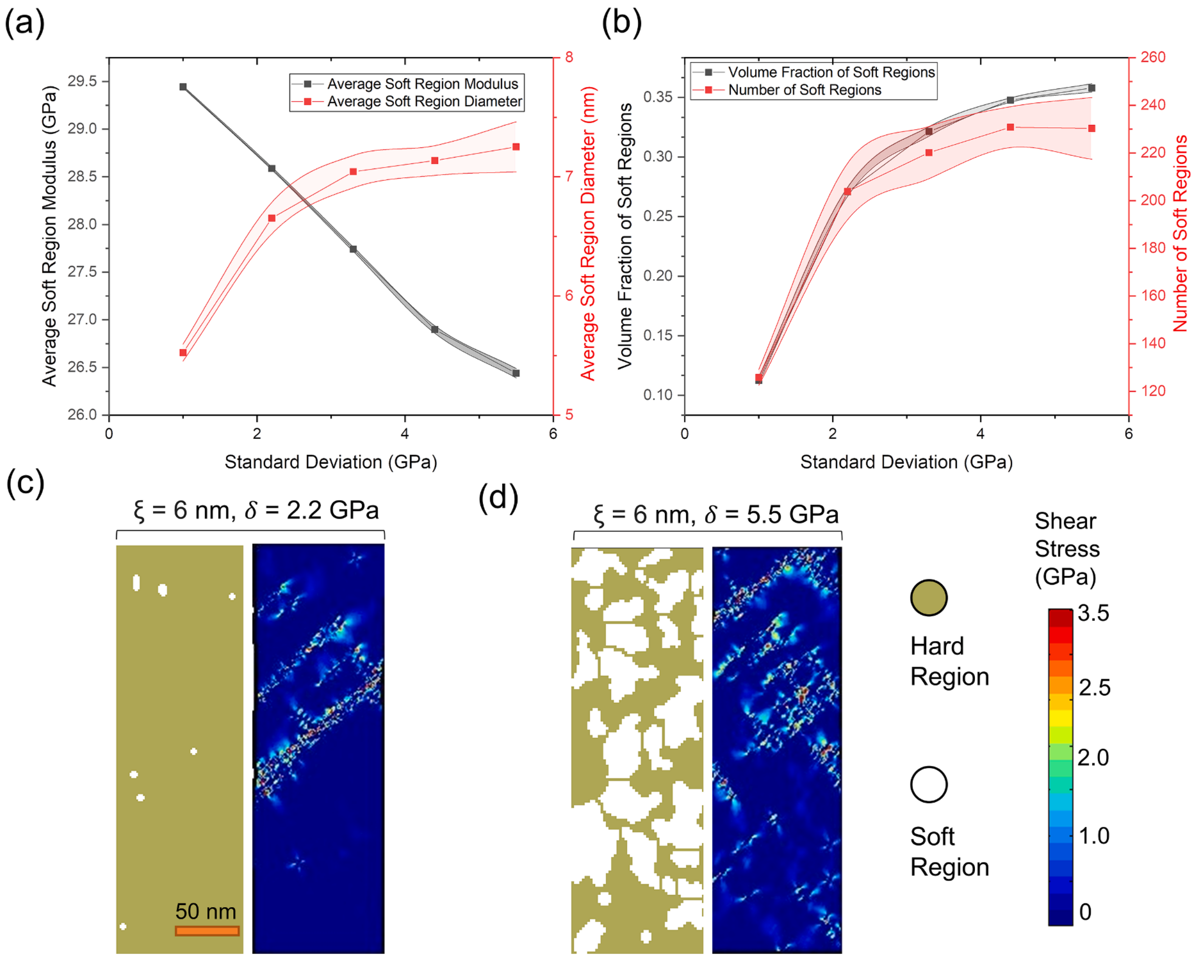

Fig. 3. The standard deviation of shear modulus distribution δ vs. characteristics of the soft regions. (a) Average soft region modulus and diameter as a function of the standard deviation of shear modulus distribution. (b) Volume fraction and the number of soft regions as a function of shear modulus distribution. (c-d) The soft regions and the corresponding local shear stress maps prior to yielding for the simulated samples with $\delta = 2.2$ GPa and $\delta = 5.5$ GPa, respectively.

2.2 GPa case and the $\delta = 5.5$ GPa case are different even though they have the same spatial correlation length $\xi = 6$ nm. There are nearly no soft regions in the $\delta = 2.2$ GPa case, while large soft regions appear in the $\delta = 5.5$ GPa case. Therefore, upon yielding, highly localized shear stress appears on the sample with the $\delta = 2.2$ GPa case, and distributed shear stress appears on the sample with the $\delta = 5.5$ GPa case.

3.3. *Effects of nanoscale heterogeneities on stress-strain responses of MGs*

The spatial heterogeneity of MGs is described by the spatial correlation length of local shear moduli. To reveal the effect of spatial heterogeneity on the mechanical response of MGs, we generated stress and strain curves of 5 samples with different spatial correlation lengths, as $\xi = 0.5$ nm, 3.0 nm, 5.0 nm, 7.0 nm, and 11.0 nm. Fig. 4(a) shows the representative stress-strain responses of these MGs. The yield stress of MGs is defined at the 0.2% offset from the stress-strain plots. For small correlation lengths, such as $\xi = 0.5$ nm, the stress drops sharply around the yielding. This sharp stress drop signifies strain localization associated with the formation of a shear band, as shown in Fig. 4(b). With increasing the spatial correlation length, the stress drops slowly, indicating a limited ductility increases as spatial heterogeneity decreases. The macroscopic stress-strain response approaches a perfect-plastic one, featuring more diffuse plastic flow as illustrated with the $\xi = 6$ nm sample in Fig. 4(c). Comparing the deformation morphology of the two samples with $\xi = 0.5$ nm and 6.0 nm, it is noticed that only a few primary shear bands develop and strain is highly localized when the correlation length is near to or smaller than the diameter of an STZ (e.g., $\xi = 0.5$ nm). The corresponding local modulus map (Fig. 4(b))

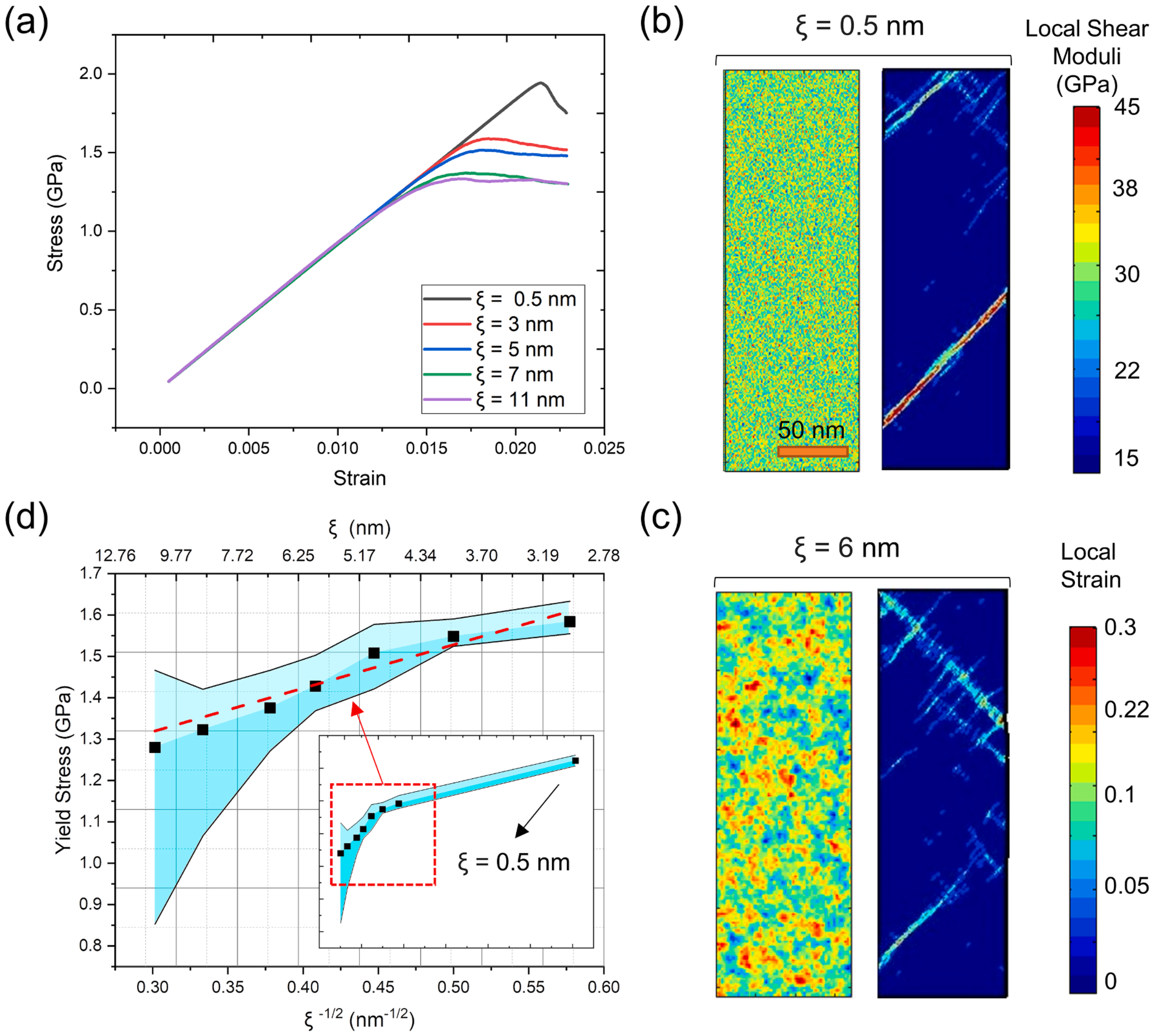

Fig. 4. The mechanical behaviors of simulated MGs at different spatial correlation lengths ξ. (a) The representative stress-strain response. (b-c) The local modulus distribution (left) and their corresponding local strain map (right) upon yielding for the samples with $\xi = 0.5$ nm vs. $\xi = 6$ nm, respectively. (d) The average yield stress as a function of correlation length, $\xi^{-1/2}$, exhibiting a Hall-Petch-like relationship.

indicates that there are no significantly large regions (i.e. larger than the size of an STZ) with a lower/higher coarse-grained shear modulus compared to the overall average. The strain localization path tends to develop from the first nucleation site rather than produce a new one, hence, only one primary shear band is formed from the strain localization. In contrast, the local shear modulus map of the sample with $\xi = 6$ nm shows significantly higher or lower local shear moduli that tend to aggregate. These regions are larger than the size of one STZ and can be viewed as hard regions in the sample. Consequently, the plastic flow proceeds in a diffuse manner, and the strain localization paths also tend to propagate through the soft regions.

Corresponding to this observation, there seems a relationship between the yield stress and the spatial correlation length. Analogous to the Hall-Petch relationship, we plot the data of the yield stress vs. the square root of spatial correlation length for the MGs that have the same Gaussian distribution with the standard deviation $\delta = 3.7 \pm 0.7$ GPa. Fig. 4(d) shows that the yield stress decreases as the correlation length ξ increases, the blue shaded area is the shaded error bar. More importantly, the yield stress scales inversely with the square root of spatial correlation length, reminiscent of the Hall-Petch relationship in polycrystalline materials (Cordero et al., 2016; Hall, 1951; Petch, 1953). As indicated by the red dashed line, the Hall-Petch-like trend becomes more evident when the spatial correlation length is larger than the diameter of the flow unit STZ. The R-square value for the Hall-Petch-like fitting is 0.9165, indicating a strong correlation between the yield stress and spatial correlation length. Note that the variation in the yield stresses increases as the correlation length increases, reflected by the enlarged blue shading domain. Such stress varication can be attributed to the fluctuations in the soft region statistics (e.g., sizes, numbers, and spatial distribution) as ξ increases. Despite the fluctuation, the spatial correlation length ξ can serve as a structural factor that relates to MG yielding. It is noteworthy that the Hall-Petch relationship appears to break down when the correlation length decreases to a certain range (e.g., 0.5 nm). The observed deviation in the Hall-Petch relationship for small correlation lengths can be attributed to the particular nature of the nanoscale heterogeneity and its influence on the deformation behavior of the MGs. At such a small correlation length, the absence of meaningful soft regions within MGs translates to a lack of STZ pile-up in these regions. This is due to the absence of sufficiently large soft regions to facilitate significant STZ accumulation. Consequently, the mechanical response of MGs with minimal elastic heterogeneities differs from those with larger correlation lengths, where the pile-up of STZs plays a more prominent role. Thereby, the Hall-Petch-like relationship does not hold when the correlation length approaches the size of a single STZ.

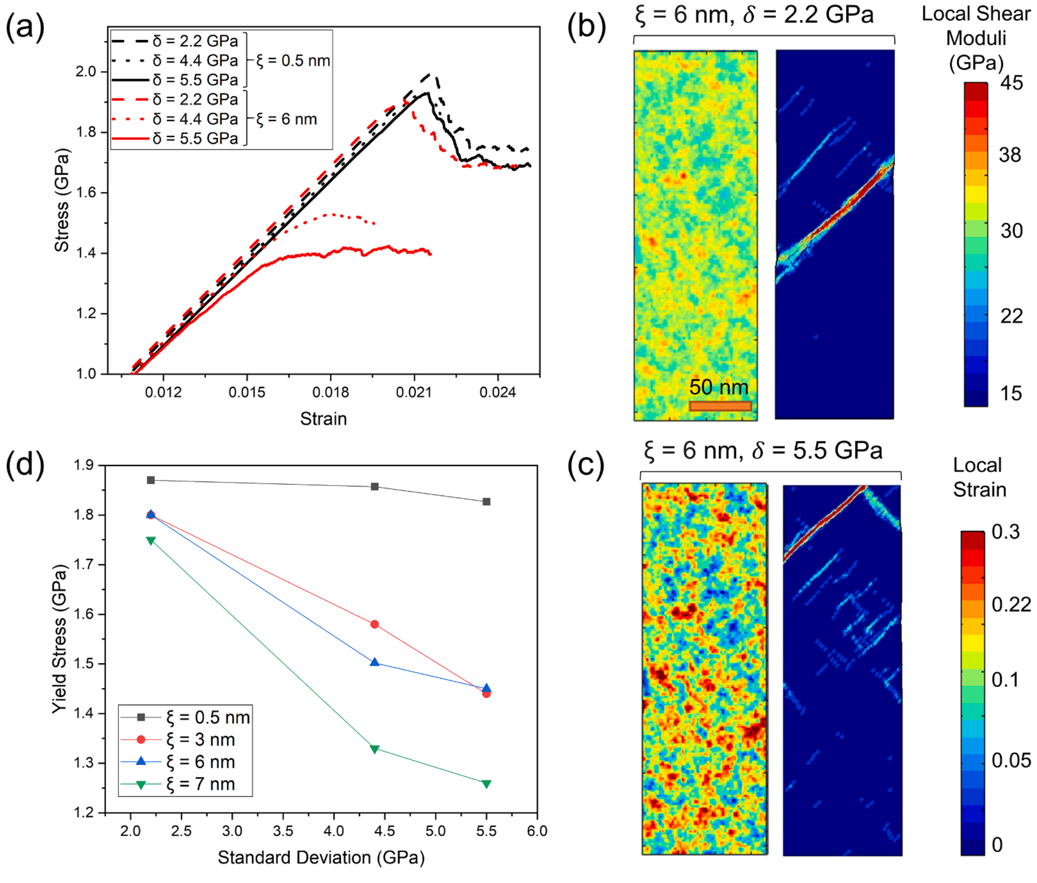

Fig. 5. The mechanical responses of the simulated MGs with various standard deviations δ of local shear moduli. (a) Representative stress-strain curves of MG samples with different δ for two spatial correlation lengths, i.e., $\xi = 0.5$ nm and 6 nm. (b-c) The local modulus distribution (left) and their corresponding local strain map (right) upon yielding for the samples with $\delta = 2.2$ GPa vs. $\delta = 5.5$ GPa, respectively. (d) Yield stress vs. standard deviation δ for MG samples with various correlation lengths.

3.4. Effects of statistical heterogeneities on stress-strain responses of MGs

Statistical heterogeneity is another critical nanostructural factor of MGs and is described by the standard deviation of the local shear modulus distribution δ. To demonstrate the statistical heterogeneity effect, we simulated two MGs with correlation lengths of 0.5 nm and 6 nm and different standard deviations $\delta = 2.2$, 4.4, and 5.5 GPa, respectively. Fig. 5(a) shows the tensile stress-strain responses of these MGs. For small correlation length, $\xi = 0.5$ nm, all the cases exhibit stress-overshoot and the yield stress is found to slightly decrease with increasing standard deviation. At a large correlation length, $\xi = 6$ nm, both the yield stress and post-yielding behavior are significantly influenced by δ. A transition from stress overshoot to nearly elastic-perfect plastic flow is observed as the standard deviation is increased from 2.2 GPa to 5.5 GPa. This is characterized by a transition of deformation modes from strain localization (Fig. 5(b)) to more diffused plastic flow (Fig. 5(c)). Using a sample with $\xi = 6$ nm as an example, the deformation morphology changes from one dominant shear band that contributes to the stress overshoot when $\delta = 2.2$ GPa (Fig. 5(b)), and to a few smaller bands when $\delta = 5.5$ GPa (Fig. 5(c)). Comparing the local shear modulus maps of these two samples, it can be observed that the extreme values of local shear moduli of $\delta = 5.5$ GPa sample are much larger than those of the $\delta = 2.2$ GPa sample, even though both samples have the same spatial characteristics (i.e. the shape and location of regions with higher or lower shear moduli). This results in a low elastic heterogeneity in the $\delta = 2.2$ GPa sample, where one primary shear band dominates plastic deformation. When δ increases to 5.5 GPa, the average local shear modulus of hard regions becomes significantly higher, while the average local shear modulus of soft regions becomes much lower than that of the whole sample. Comparing Fig. 5(b) and (c), the sample with $\delta = 5.5$ GPa displays a broader distribution of moduli. Local modulus can have values as much as approximately 30% higher or lower compared to the sample with $\delta = 2.2$ GPa. Since soft regions are regions where low local shear moduli aggregate together, the increase of δ leads to a lower average shear modulus of soft regions. Consequently, strain localization tends to initiate in different regions with significantly lower shear moduli, developing into multiple small shear bands, which diffuse plastic flow.

A closer examination of the yield stress as a function of δ for the samples with different correlation lengths is illustrated Fig. 5(d). The yield stress of all samples decreases as δ increases, the rate of such decrease, however, increases with correlation length. The $\xi = 0.5$ nm sample experiences only a slight change in yield stress when δ increases from 2.2 GPa to 5.5 GPa, whereas the yield stress of the $\xi = 6$ nm sample drops by over 25%. In general, the samples with larger correlation lengths exhibit a greater loss in strength with increasing δ compared to samples with smaller correlation lengths.

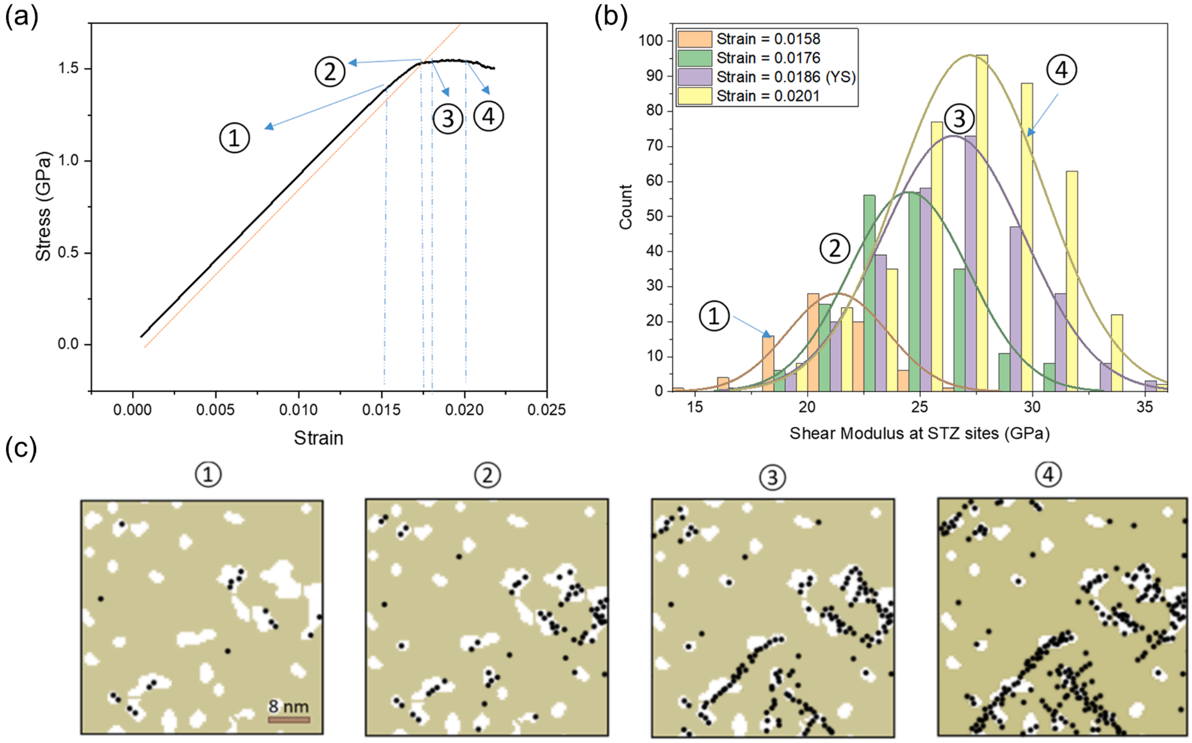

Fig. 6. The yielding process of a representative heterogeneous MG with $\xi = 4$ nm. (a) The stress-strain curve, along with the four critical moments labeled. (b) The evolution of the distributions of the shear moduli of the activated STZ sites at four critical moments. (c) Locations of activated STZs overlap on locations of soft regions at four critical moments.

4. Discussion

4.1. Deformation mechanisms of MGs in the presence of nanoscale heterogeneity

Furthermore, the macroscopic yielding results from the percolation of STZs from soft regions to hard regions in the MG with nanoscale heterogeneity. Taking the sample with $\xi = 4$ nm as an example, Fig. 6(a) reveals four critical moments corresponding to the stress-strain curve, namely, prior to yielding in microplasticity, near yielding, at yielding, and post-yielding. The distributions of the shear moduli of activated STZ sites at the four critical moments are shown in Fig. 6(b). Note that as strain increases, more potential STZ sites with higher local shear moduli are activated, and the average shear modulus of the activated STZs also increases. Fig. 6(c) displays the locations of the activated STZ sites on top of the spatial distribution of the soft and hard regions at the four moments. Before macroscopic yielding, all the activated STZs are nearly in the soft regions. Near yielding, a few STZs are activated outside the soft regions, and most recently activated STZs are near the edges of soft regions. At yielding, a few incipient shear bands are formed by STZs percolating into the hard regions that connect different soft regions. Post-yielding, there is an increased probability of STZ activations occurring in hard regions, and the incipient shear bands are developing with more STZs activated in the hard regions along the strain localization path. Therefore, the percolation of STZs from soft regions to hard regions is the essential moment of the transition from micro to macro plasticity.

We further resolve the activation sequence by tracing STZs in a single representative large soft region from zero strain to macroscopic yielding. During the activation process, 20 STZs are identified, which are labeled in numerical order based on the sequence in Fig. 7(a). Although the activation of the STZs remains stochastic in nature, soft regions are preferred initiation sites. STZs are activated in a gradual manner forming a shear band localized to the soft region prior to yielding. To determine the shear modulus of each activated STZ, a three-step process is employed. Firstly, the STZ activation sequence list is extracted from the simulation, focusing on the region of interest. Secondly, the positions of each activated STZ are located on the finite element mesh, and their corresponding element numbers are identified. Finally, the values of the moduli assigned to the elements associated with each activated STZ are obtained. As shown in Fig. 7(b), before yielding, the activated STZs are always located in a region where the local shear modulus is lower than the average shear modulus. When the activated STZ is located in a region with a local modulus close to the average modulus, the following activation tends to occur in a region with a lower local shear modulus. Upon macroscopic yielding, the STZs start to activate in the hard regions. As more STZs become active in the soft regions, stress concentration at the boundary between soft and hard regions intensifies. This heightened stress concentration enables STZs in the harder regions near the boundary to accumulate enough stress to overcome the higher activation energy barrier. Statistically, the percolation of STZs from soft to hard regions leads to the macroscopic yielding of MGs.

4.2. A Super-STZ model

The yielding behavior of heterogeneous MGs features continuous activation of numerous STZs along the shear path throughout the soft regions, and the yielding occurs corresponding to the percolation of STZs into the hard regions. Illustrated in Fig. 8(a), during the deformation of MG, the activation of multiple STZs along the shear plane leads to the development of stress concentrations. This array of activated STZs transforms the stress field from the original quadrupole pattern exhibited by an individual STZ to a dipole pattern. In the scenario, prior to yielding, the STZ initially forms in the soft region, and then additional STZs appear one by one in the vicinity of the formed STZs as a result of stress redistribution. The continuous accumulation of the activated STZs in a soft region forms a "Super-STZ" as shown in Fig. 8(b). This can be viewed as an Eshelby transition-like process, as more STZs are being activated, the Super-STZ growth and the stresses can concentrate in its tip regions. It is anticipated that the stress concentration built up in front of the Super-STZ facilitates the breakthrough of Super-STZ into a hard region, leading to macroscopic yielding. Such yielding behavior of the heterogeneous MGs is reminiscent of the dislocation pile-up and grain boundary strengthening in the crystalline materials. As illustrated in Fig. 8(c) of a dislocation pile-up model (Cottrell and Bilby, 1949; Eshelby et al., 1951), a dislocation source within a grain produces a significant number of dislocations. As the leading dislocation encounters a grain boundary, it comes to a stop, leading to the dislocation

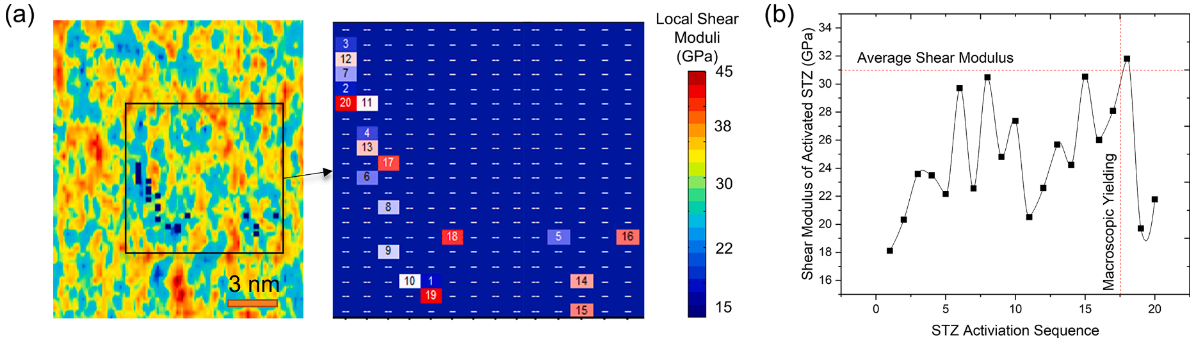

Fig. 7. (a) The STZ activation sequence inside a soft region up to macroscopic yielding in the sample with ξ=4 nm. (b) The local shear moduli of the activated STZs in sequence.

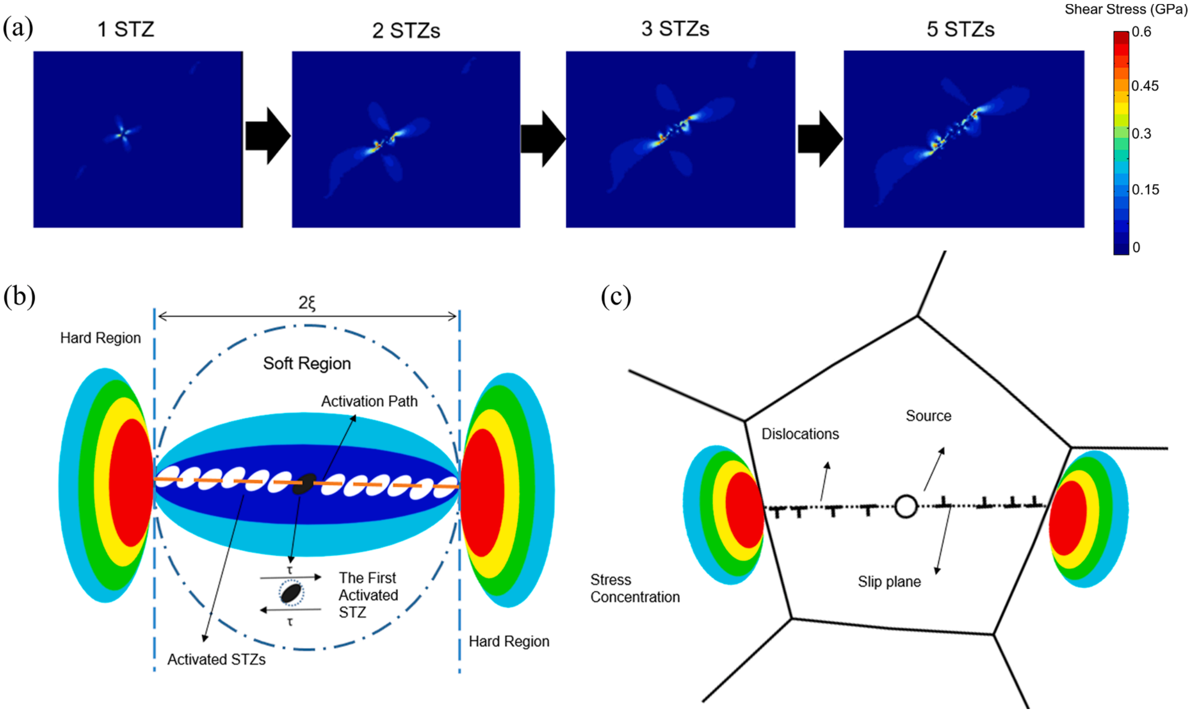

Fig. 8. (a) Evolution of shear stress field as multiple STZs are activated along the shear plane, forming an array of STZs, i.e., Super-STZ. (b) Schematic of STZ accumulation that forms a Super-STZ and results in stress concentration. (c) Schematic of the dislocation pile-up model in polycrystalline metals.

pile-up. The accumulation of dislocations results in a high dislocation density in that region. The front dislocation experiences stress concentration due to the combined stress fields of the piled-up dislocations (Anderson et al., 2017). The stress concentration plays a crucial role and assists the dislocation to break through the resistance imposed by the grain boundary, which governs yield stress. Meanwhile, in our study of MGs shown in Fig. 8(b), the soft regions behave like grains, and the elastic contrast between soft and hard regions acts like grain boundaries, providing a barrier for the spatial correlation of STZs to form shear bands. As deformation progresses, multiple STZs are activated along the shear plane, forming an array of STZs or Super-STZ. The growth of a Super-STZ and the stress concentration in its front further resemble the stress concentration observed in dislocation pile-up. The anticipated breakthrough

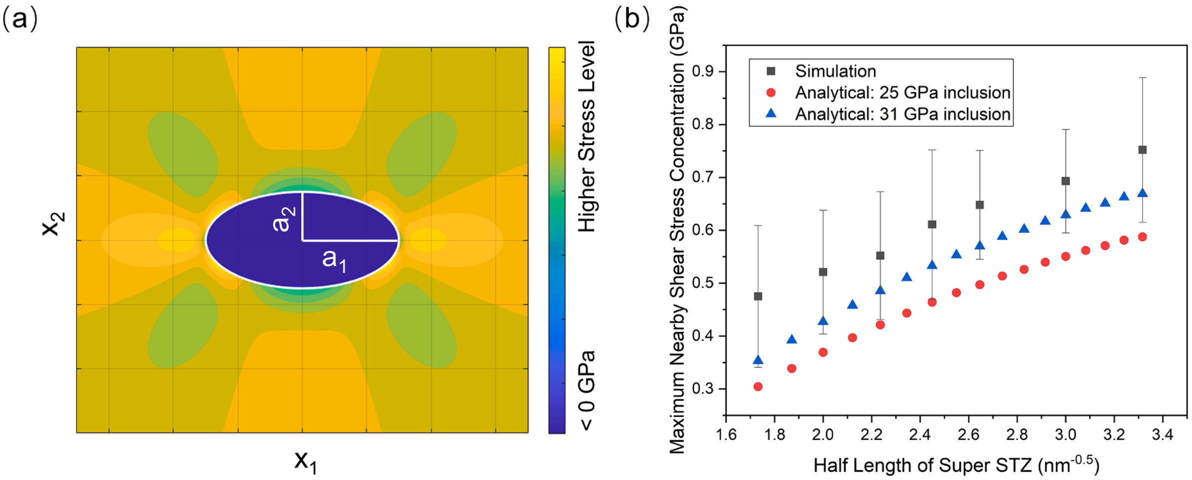

Fig. 9. The Super-STZ model. (a) A representative shear stress field upon a Super-STZ transition. (b) Maximum shear stress concentration in front of a Super-STZ vs. square root of half-length of Super STZ by solving Eq. (8) of Super-STZ model, where matrix in all cases has a shear modulus of 31 GPa. For comparison, the simulated data are included by measuring the maximum shear stress near the end of a shear band within a soft region at macroscopic yielding for simulated MGs with different correlation lengths.

of the Super-STZ into a hard region, leading to macroscopic yielding, signifies the progression of deformation beyond localized regions to a more extensive and global deformation. This can be compared to the concept of yielding in dislocation pile-up, where the resistance offered by the grain boundary is eventually overcome, resulting in plastic deformation and yielding at a macroscopic level.

Furthermore, we quantify the stress concentration in front of the Super-STZ using the Eshelby inclusion model (Eshelby, 1957). The Super-STZ formed by an ideal array of activated STZs within a soft region is modeled as an ellipsoidal inclusion within an infinite, isotropic matrix. As the 2D STZ dynamics simulations adopt a plain strain condition, a closed-form, plane-strain solution proposed by Jin et al. (2011) for the case of an elliptic cylinder is implemented to compute the exterior elastic stress fields around the inclusion. The implemented code is validated against analytical benchmark cases presented by Meng et al. (2012). More specifically, the exterior elastic stress field about the inhomogeneous inclusion, σ_{ij}, is solved according to Hooke's law as

$$\sigma_{ij} = C_{ijkl} G_{klmn} \epsilon^{**}_{mn} \tag{7}$$

where C_{ijkl} is the isotropic elastic stiffness tensor of the matrix (hard region), G_{klmn} is the exterior-point Eshelby tensor for an elliptic cylindrical inclusion provided by Jin et al. (2011), and ϵ^{**}_{mn} is the equivalent eigenstrain the inclusion is subjected to if there were no elastic mismatch (Mura, 2013). The case of the elliptic cylindrical inclusion is retrieved from the ellipsoidal inclusion case by letting one of the three principal semi-axes of the ellipsoid tend toward infinity (e.g. $a_3 \rightarrow \infty$) while the remaining principal semi-axes are finite ($a_1 = a$, $a_2 = b$). A schematic of the elliptic cylindrical inclusion problem and the orthogonal reference coordinate frame is presented in Fig. 9(a). Here, the Super-STZ array is assumed to have activated along the direction of maximum shear stress aligned with the tensile axis (i.e. 45° rotation about the tensile axis). As such, the local stress concentration resulting from the applied eigenstrain to the inclusion may be solved in this rotated frame. The first principal semi-axis, a_1, aligned with the x_1 axis represents the half-length of the Super-STZ array, which is estimated as the soft region size and varied from 3 nm to 11 nm. The second principal semi-axis, a_2, aligned with the x_2 axis represents half of the length of the STZ size and is fixed at 1.5 nm. An initial eigenstrain, ϵ^{*}_{12}, equal to the characteristic shear strain, γ_0, is applied to the elliptic cylindrical inclusion without the application of remote stress, and the inhomogeneity problem is solved by the integration of the Equivalent Inclusion Method (Eshelby, 1957; Mura, 2013) into the closed-form solution of Jin et al. (2011). A quadrupolar shear stress field results from a combination of the elastic mismatch between the soft (inclusion) and hard (matrix) regions of the MG and the eigenstrain deformation (Şopu et al., 2020b; Sun et al., 2016). As $a_1 > a_2$ for all cases considered here, the maximum long-ranging shear stress concentration can be found along the x_1 axis ($|x_1| > a_1, x_2 = 0$) and an analytical solution is derived utilizing the exterior-point Eshelby tensor of Jin et al. (2011). The maximal shear stress along the x_1 axis is found as

$$\sigma_{12} = 2\mu_{matrix} G_{1212\left(x_{1,crit},\ x_2=0\right)}\ \epsilon^{**}_{12} \tag{8}$$

where σ_{12} is the shear stress about the inclusion, μ_{matrix} is the shear modulus of the (harder) matrix, G_{1212} is a term from the exterior-point Eshelby tensor derived by Jin et al. (2011), and ϵ^{**}_{12} is the equivalent eigenstrain which encompasses both the characteristic shear strain applied to the inclusion during the transformation and the elastic contrast between the inclusion and the matrix. When solved where $x_1 = x_{crit}$ and $x_2 = 0$, the analytical solution is for the maximal shear stress near the "tip" of the Super-STZ array.

Fig. 9(b) compares the trend of maximal long-ranging shear stress concentration as a function of the square root of a_1 for both the simulated results and the Super-STZ model. The simulation results are obtained by measuring the maximum shear stress near the end of a shear band within a soft region at macroscopic yielding for simulated MGs with different correlation lengths. To enhance the statistical significance, the stress concentration of several soft regions is extracted for the samples with the same correlation length. Furthermore, we utilize Eq. (8) for a given correlation length (i.e., inclusion shape) and inclusion stiffness (embedded into ϵ^{**}_{12}) in order to solve for the analytical shear stress concentration at the tip of the Super-STZ. The solutions of Eq. (8) for various cases produce the data points in Fig. 9(b) marked "Analytical". It is observed that there is good agreement between the simulated data and analytical results in both trends and magnitude. As the length of Super STZ inclusion increases, corresponding to an increase in the number of activated STZs in the array, the local shear stress concentration near the tip of the inclusion also increases. This can be attributed to the interactions of elastic stress fields from the individual shearing of multiple STZs in the soft region, leading to an overall higher local shear stress. This increase in shear stress near the tip, or the "leading" activated STZ in the array, creates a localized region of elevated shear stress that can decrease the local energy barrier and facilitate higher activation rates for nearby STZs in the hard region, initiating the process of strain percolation in the system. Note that there exists some variation in the stress concentration from simulations, which can be attributed to the simulated MG's non-binary nature. Unlike binary MGs in the analytical model with only two modulus values, the simulated MGs have a gradient structure, meaning they possess a wide range of moduli values across the model. Additionally, stress fields of different soft regions in the simulated MGs sometimes overlap, further contributing to the variation in stress levels. The Super-STZ model, by construction, is attempting to idealize an otherwise stochastic activation process by extending the existing Eshelby form to capture the linear array-like activation paths observed in soft regions of our model MGs. The assumption that a soft inclusion (Super-STZ array) is interacting with a harder matrix (i.e., a hard region surrounding a soft region) asserts that the shear stress concentration obtained from the analytical solution is the idealized condition that occurs at yielding where the transition to macroscopic plasticity is in line with the percolation of the shear bands from the softer regions into the harder regions. Fig. 9(b) supports this by comparing the analytical solution of tip shear stress concentration, obtained using Eq. (8), for various correlation lengths to shear stress values directly sampled from shear stress fields of the simulated MGs. Both the magnitude and qualitative trend between simulated data and analytical results show reasonable agreement despite the simplified nature of the Super-STZ model construction and the inherently stochastic nature in the simulations, therefore the Super-STZ model is justified in its use to understand how the onset of macroscopic plasticity manifests in our model MGs.

4.3. The Hall-Petch-like relationship

Based on the stress concentration in the Super-STZ model, we formulate a Hall-Petch-like equation that relates the yield stress of heterogenous MG to the spatial correlation length ξ and standard deviation δ of the nanoscale heterogeneity, given as:

$$\sigma_y = \sigma_0 + \frac{kl^{1/2}\delta}{\xi^{1/2}} \tag{9a}$$

$$\text{where } \sigma_0 = a\overline{\mu} - b\delta \tag{9b}$$

where σ_0 is a reference stress when the spatial correlation length approaches infinity, l is the radius of an STZ, k is a material constant, and $\overline{\mu}$ is the average shear modulus of the heterogeneous MG. The reference stress σ_0 is proportional to the average shear modulus but negatively proportional to the standard deviation δ increases, with a and b being the two fitting parameters. The spatial correlation length ξ exhibits a linear relationship with the average soft region size, and the standard deviation δ is directly proportional to the elastic mismatch. According to the Super-STZ model, the required yield stress σ_y, which is magnified by the stress concentration, therefore, scales with δ but inversely with $\xi^{1/2}$. It's noteworthy that the standard deviation δ plays a dual role in influencing the yield stress σ_y as outlined in Eq. (9a). This relationship encompasses two essential components: the reference stress σ_0, reflective of uniformity, and the stress concentration arising from spatial heterogeneity. In the absence of spatial heterogeneity in Eq. (9b), the yield stress decreases as δ increases due to the increasing probability of the participation of soft elements for shear band nucleation. The stress concentration, captured in the second term of Eq. (9a), is inversely linked to δ, representing the elastic mismatch's extent. As δ decreases, stress concentration magnifies, impacting the applied stress required for yielding. The Super-STZ model implies that a smaller elastic mismatch yields a higher stress concentration. Consequently, a lower applied stress becomes necessary for STZs to propagate from soft to hard regions, resulting in macroscopic yielding. Conversely, the stress concentration is proportionate to $\xi^{1/2}$, leading to the inverse scaling of the applied stress necessary for yielding with $\xi^{1/2}$, representing the second term in Eq. (9a).

Fig. 10(a) illustrates the influence of the standard deviation δ on yield stress. The trend of linearly decreasing yield stress with increasing standard deviation, while keeping the correlation length constant, aligns with the relationship described by Eq. (9). To ensure result convergence, we have conducted an additional set of 24 simulations due to the higher yield stress fluctuation observed with larger correlation lengths compared to smaller ones. A correlation length of 11 nm, notable for its significant yield stress fluctuation, was selected for examination. Four standard deviations of the local modulus distribution, namely, 2.2 GPa, 3.7 GPa, 4.3 GPa, and 4.9 GPa, were chosen. The results, depicted in Fig. 10(a), reveal that even at the largest correlation length, yield stress changes for each standard deviation are relatively small. The 2.2 GPa, 3.7 GPa, 4.3 GPa, and 4.9 GPa groups exhibit coefficient of variation (CV) values of 1.25%, 5.22%, 4.73%, and 1.69%, respectively. Notably, the 3.7 GPa and 4.3 GPa groups display higher yield stress variations than both lower and higher standard deviation groups. Interestingly, an outlier emerges within the 3.7 GPa group according to the 1.5 times interquartile range (IQR) criterion. This aligns with prior observations (Gu et al., 2022) that stress-driven strain percolation becomes more likely when soft regions are either small (2.2 GPa group) or excessively large (4.9 GPa group). Such percolation mitigates the nanostructural impact on shear banding, reducing yield stress fluctuations. Moreover, these findings suggest that the Hall-Petch-like fitting equation may introduce greater uncertainty in scenarios of intermediate structural heterogeneity. Complex nanostructures in model MGs contribute to statistical uncertainty, influencing shear banding behavior and resulting in structure-influenced strain localization, subsequently impacting yield stress.

We then apply Eq. (9) to fit all the simulated yield stresses with different degrees of nanoscale heterogeneities (~80 cases). The obtained parameters are $a = 0.06$, $b = 0.16$, and $k = 0.15$, with an R-squared value of 0.745, as shown in Fig. 10(b). The Hall-Petch-like

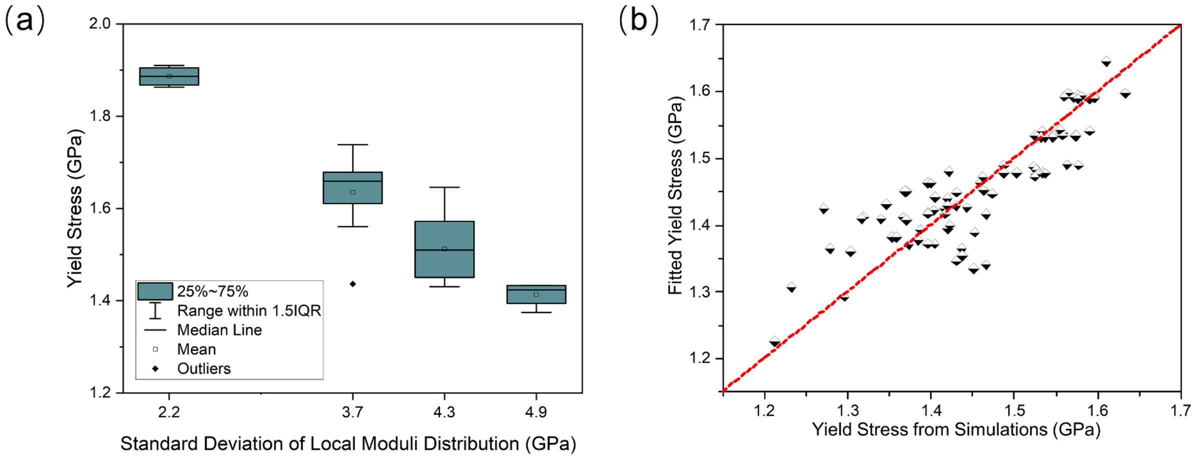

Fig. 10. (a) Impact of local modulus distribution standard deviations on yield stress fluctuation of model MGs with 11 nm correlation length. (b) The fitted yield stress using Eq. (9) vs. the simulated yield stress of MGs with various degrees of nanoscale heterogeneities.

equation demonstrates strong agreement with the simulated data across the majority of cases. However, it exhibits increased error in situations where the MG model incorporates more complex nanostructures, consequently introducing a level of statistical uncertainty. Moreover, having a value of $a = 0.06$, which establishes a relationship between the reference stress σ_0 and the average shear modulus, follows a universal criterion for the plastic yielding of MGs (Johnson and Samwer, 2005).

The simplicity of the material parameters employed in the equation suggests its potential transferability across different systems. We conduct further validation of Eq. (9) using experimental data of $Zr_{53}Cu_{36}Al_{11}$ MGs, as documented by Zhu et al. (2018). In this validation, the mechanical properties of five different $Zr_{53}Cu_{36}Al_{11}$ samples were characterized through instrumented nanoindentation. In the experimental study, the spatial heterogeneity in a $Zr_{53}Cu_{36}Al_{11}$ MGs was observed in a series of hyper-quenched samples and subjected to annealing at 553 K, roughly 0.8 times the glass transition temperature (T_g). These samples underwent varying annealing durations ranging from 0 to 720 min, resulting in a variation in the material's microstructure. To determine the correlation length associated with spatial heterogeneity, high-angle annular dark-field scanning transmission electron microscopy (HAADF-STEM) was employed to observe patterns of inhomogeneous contrast. The characteristic size of dark regions in these images serves as a metric for the spatial heterogeneity's correlation length, which was observed to decrease as annealing time increases. Furthermore, the sizes of dark regions as determined from HAADF-STEM images align closely with the characteristic spatial heterogeneity lengths measured using AM-AFM. Mechanical properties, such as hardness and Young's modulus of samples with varying spatial heterogeneity were determined using nanoindentation. Each sample was subjected to measurements at twenty-five points to derive both the mean values and the standard deviation for the measured mechanical properties.

In this validation process, several assumptions have been made. Firstly, we assume a Poisson's ratio of 0.36 for all samples and use this Poisson's ratio to calculate the shear modulus of each sample based on experimentally measured Young's modulus. Secondly, we consider a constant STZ size of 1.5 nm in the experiments, close to the value in our simulation and within the range of reported values. Lastly, we employ a simplified approach by using experimental hardness divided by 3 as a rough estimate of the yield stress for each sample. All parameters used in this validation are summarized in Table 2.

We perform a fitting procedure on the data summarized in Table 2 using Eq. (9). The parameters obtained from the fitting are as follows: $a = 0.053$, $b = 0.197$, and $k = 0.317$. This fitting shows a high level of accuracy, as indicated by the R-squared value of 0.983. Utilizing the experimental findings comes with certain limitations. Notably, the standard deviation from nanoindentation, which is used as a proxy for local modulus distribution, may not fully represent the variability in moduli across the entire sample. This limitation arises due to the constraints of the measurement process, wherein only 25 points are sampled for each sample, and the indenter size is relatively large, yielding an average result over a micrometer-scale region. Furthermore, the correlation length obtained from the measurements in HAADF-STEM images is different compared to the spatial correlation length of local moduli used in simulations, given that the former aligns more closely with the dimensions of the soft regions. Despite these limitations, the experimental validation still offers promising results. As illustrated in Fig. 11, the calculated yield stress, derived from the fitted equation, closely aligns with the actual yield stress obtained from the experiments, falling well within the error bars. The mean absolute percentage errors between the fitted yield stress and the actual yield stress consistently remain below 1%, reinforcing the generality and applicability of Eq. (9).

Our study's foundation lies in the STZ model (Argon, 1979) considering STZs as fundamental units of deformation. This basis gives rise to the observed structure-property relationship in nanoscale MGs. The general validity of the Hall-Petch-like relationship, connecting yield stress and spatial heterogeneity, is anticipated for MGs exhibiting STZ characteristics and nanoscale heterogeneity. The concept of STZ percolation and Super-STZ array formation holds relevance for heterogeneous microstructures in diverse MG systems. Nevertheless, the dynamic nature of real MGs could influence this relationship due to the interplay between glass structure evolution and STZs in varying systems. Furthermore, while our simulations are limited to two dimensions, it's important to recognize that shear banding behavior is more complex in three-dimensional systems. Transitioning from 2D to 3D can impact STZ connectivity and interactions with heterogeneities in bulk metallic glasses (BMGs). Despite these limitations, our focus remains on gleaning valuable insights into how spatial heterogeneity influences MG yielding and deformation mechanisms. The derived Hall-Petch-like relationship is 2D-based, and adapting it to 3D BMGs would require careful consideration of geometric and mechanical distinctions. To comprehensively ascertain the applicability of our findings, a synergistic approach combining modeling and experimentation is imperative. Thus, the derived Hall-Petch-like equation encapsulates pivotal structural factors influencing heterogeneous MGs' yielding and offers insights for guiding nanostructure design in amorphous alloys.

5. Conclusions

In this study, we have investigated the yielding and deformation behaviors of heterogenous MGs using a mesoscale STZ dynamics model by tuning the spatial correlation and standard deviation of local shear moduli on the nanoscale. A Hall-Petch-like relationship has been identified between the yield stress and spatial correlation length, where the yield stress of heterogenous MG scales inversely with the square root of the correlation length. Such yielding behavior results from the influence of nanoscale heterogeneity on the structural characteristics, in particular, the size and strength of the soft regions, and the connection between the soft region characteristics and shear banding mechanisms. We have found that the percolation of STZs from soft to hard regions is the critical moment for MG yielding in the presence of structural heterogeneity. Prior to yielding, the STZs activate and accumulate inside soft regions and form a Super-STZ, a scenario similar to the dislocation pile-up at the grain boundary in the polycrystal. The stress concentration built up in the front of the Super-STZ follows a square root relationship with the size of soft regions, and the slope of the relationship decreases with modulus mismatch between Super-STZ and matrix. Based on the Super-STZ model, a Hall-Petch-like equation has been derived, which quantifies the yield of MGs with the spatial correlation length and standard deviation of the nanoscale heterogeneity. Our study provides a mechanistic understanding of the yielding and deformation behaviors in heterogenous MGs, indicating that local

Table 2
Properties of $Zr_{53}Cu_{36}Al_{11}$ samples (Zhu et al., 2018).

Sample	ξ (nm)	$\overline{\mu}$ (GPa)	δ (GPa)	σ_y (GPa)
1	2.78	38.10	0.52	2.04
2	3.70	37.24	0.29	1.98
3	4.53	36.29	0.50	1.93
4	4.94	36.08	0.58	1.91
5	5.95	35.93	0.52	1.88

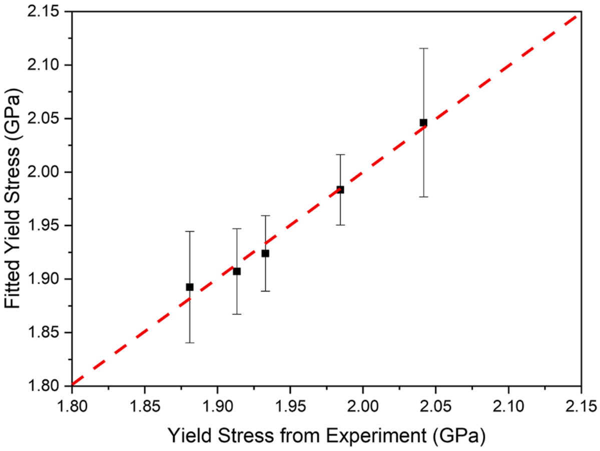

Fig. 11. The fitted yield stress using Eq. (9) vs. actual yield stress with error bars adapted from experimental data (Zhu et al., 2018).

heterogeneity can be an important structural factor that quantifies large-scale mechanical properties.

CRediT authorship contribution statement

Yucong Gu: Formal analysis, Investigation, Data curation, Writing – original draft, Visualization. **Jonathan Cappola:** Formal analysis, Investigation, Writing – original draft. **Jian Wang:** Conceptualization, Resources, Writing – review & editing, Funding acquisition. **Lin Li:** Conceptualization, Methodology, Resources, Writing – review & editing, Project administration, Funding acquisition.

Declaration of Competing Interest

The authors declare that they have no known competing financial interests or personal relationships that could have appeared to influence the work reported in this paper.

Data availability

Data will be made available on request.

Acknowledgments

This work is supported by the US National Science Foundation (Grant No. CMMI-1727875 and CMMI- 2132336/2132383). This work used Anvil CPU and GPU at Purdue through Allocation No. MAT210034 from the Advanced Cyberinfrastructure Coordination Ecosystem: Services & Support (ACCESS) program.

References

An, Q., Samwer, K., Demetriou, M.D., Floyd, M.C., Duggins, D.O., Johnson, W.L., Goddard III, W.A., 2016. How the toughness in metallic glasses depends on topological and chemical heterogeneity. Proc. Natl. Acad. Sci. 113, 7053–7058.
Anderson, P.M., Hirth, J.P., Lothe, J., 2017. Theory of Dislocations. Cambridge University Press.
Argon, A., 1979. Plastic deformation in metallic glasses. Acta Metall. 27, 47–58.
Bian, X., Şopu, D., Wang, G., Sun, B., Bednarčik, J., Gammer, C., Zhai, Q., Eckert, J., 2020. Signature of local stress states in the deformation behavior of metallic glasses. NPG Asia Mater. 12, 1–10.

Bulatov, V., Argon, A., 1994. A stochastic model for continuum elasto-plastic behavior. I. Numerical approach and strain localization. Model. Simul. Mater. Sci. Eng. 2, 167.

Callister, W.D., 2000. Fundamentals of Materials Science and Engineering. Wiley, London.

Cheng, Y., Ma, E., 2009. Configurational dependence of elastic modulus of metallic glass. Phys. Rev. B 80, 064104.

Chiles, J.P., Delfiner, P., 2012. Geostatistics: Modeling Spatial Uncertainty. John Wiley & Sons.

Cordero, Z.C., Knight, B.E., Schuh, C.A., 2016. Six decades of the Hall–Petch effect–a survey of grain-size strengthening studies on pure metals. Int. Mater. Rev. 61, 495–512.

Cottrell, A.H., Bilby, B.A., 1949. Dislocation theory of yielding and strain ageing of iron. Proc. Phys. Soc. London Sect. A 62, 49.

Das, A., Dufresne, E., Maaß, R., 2020. Structural dynamics and rejuvenation during cryogenic cycling in a Zr-based metallic glass. Acta Mater. 196, 723–732.

Di, S., Ke, H., Wang, Q., Zhou, J., Zhao, Y., Shen, B., 2022a. Large tensile plasticity induced by pronounced β-relaxation in Fe-based metallic glass via cryogenic thermal cycling. Mater. Des. 222, 111074.

Di, S., Wang, Q., Yang, Y., Liang, T., Zhou, J., Su, L., Yin, K., Zeng, Q., Sun, L., Shen, B., 2022b. Efficient rejuvenation of heterogeneous {[(Fe0. 5Co0. 5) 0.75 B0. 2Si0. 05] 96Nb4} 99.9 Cu0. 1 bulk metallic glass upon cryogenic cycling treatment. J. Mater. Sci. Technol. 97, 20–28.

Di, S., Wang, Q., Zhou, J., Shen, Y., Li, J., Zhu, M., Yin, K., Zeng, Q., Sun, L., Shen, B., 2020. Enhancement of plasticity for FeCoBSiNb bulk metallic glass with superhigh strength through cryogenic thermal cycling. Scr. Mater. 187, 13–18.

Ding, J., Cheng, Y.Q., Ma, E., 2014a. Full icosahedra dominate local order in Cu64Zr34 metallic glass and supercooled liquid. Acta Mater. 69, 343–354.

Ding, J., Li, L., Wang, N., Tian, L., Asta, M., Ritchie, R., Egami, T., 2021. Universal nature of the saddle states of structural excitations in metallic glasses. Mater. Today Phys. 17, 100359.

Ding, J., Patinet, S., Falk, M.L., Cheng, Y., Ma, E., 2014b. Soft spots and their structural signature in a metallic glass. Proc. Natl. Acad. Sci. 111, 14052–14056.

Du, Y., Han, W., Zhou, Q., Xu, Y., Zhai, H., Bhardwaj, V., Wang, H., 2020. Enhancing the plasticity of a Ti-based bulk metallic glass composite by cryogenic cycling treatments. J. Alloys Compd. 835, 155247.

Duan, G., Lind, M.L., Demetriou, M.D., Johnson, W.L., Goddard III, W.A., Çağin, T., Samwer, K., 2006. Strong configurational dependence of elastic properties for a binary model metallic glass. Appl. Phys. Lett. 89, 151901.

Eshelby, J., Frank, F., Nabarro, F., 1951. The equilibrium of linear arrays of dislocations. The London, Edinburgh, and Dublin Philosophical Magazine and. J. Sci. 42, 351–364.

Eshelby, J.D., 1957. The determination of the elastic field of an ellipsoidal inclusion, and related problems. Proc. R. Soc. Lond. A Math. Phys. Sci. 241, 376–396.

Fan, Y., Iwashita, T., Egami, T., 2014. Evolution of elastic heterogeneity during aging in metallic glasses. Phys. Rev. E 89, 062313.

Gong, P., Yin, G., Jamili-Shirvan, Z., Ding, H., Wang, X., Jin, J., 2020. Influence of deep cryogenic cycling on the rejuvenation and plasticization of TiZrHfBeCu high-entropy bulk metallic glass. Mater. Sci. Eng. A 797, 140078.

Greer, A., Cheng, Y., Ma, E., 2013. Shear bands in metallic glasses. Mater. Sci. Eng. R Rep. 74, 71–132.

Gu, Y., Han, X., Yan, F., Li, L., 2022. The strain rate sensitivity of heterogeneous thin film metallic glasses: interplay between nanoscale heterogeneity and dynamic plasticity. Front. Mater. 9, 925096.

Hall, E., 1951. The deformation and ageing of mild steel: III discussion of results. Proc. Phys. Soc. London Sect. B 64, 747.

Han, X., Gu, Y., Yao, Y., Kong, L., Li, L., Yan, F., 2023. Processing induced nanoscale heterogeneity impact on the mechanical and electrical behavior of Cu–Zr thin film metallic glasses. Results Surf. Interfaces 10, 100094. https://doi.org/10.1016/j.rsurfi.2022.100094.

Hao, Q., Lyu, G., Pineda, E., Pelletier, J., Wang, Y.J., Yang, Y., Qiao, J., 2022. A hierarchically correlated flow defect model for metallic glass: universal understanding of stress relaxation and creep. Int. J. Plast. 154, 103288.

Homer, E., Rodney, D., Schuh, C., 2010. Kinetic Monte Carlo study of activated states and correlated STZ activity during the deformation of an amorphous metal. Phys. Rev. B Condens. Matter Mater. Phys. 81, 1–11.

Homer, E.R., Schuh, C.A., 2009. Mesoscale modeling of amorphous metals by shear transformation zone dynamics. Acta Mater. 57, 2823–2833.

Hwang, J., Melgarejo, Z., Kalay, Y.E., Kalay, I., Kramer, M.J., Stone, D., Voyles, P., 2012. Nanoscale structure and structural relaxation in Zr 50 Cu 45 Al 5 bulk metallic glass. Phys. Rev. Lett. 108, 195505.

Jiang, F., Jiang, M., Wang, H., Zhao, Y., He, L., Sun, J., 2011. Shear transformation zone volume determining ductile–brittle transition of bulk metallic glasses. Acta Mater. 59, 2057–2068.

Jiang, M., Ling, Z., Meng, J., Dai, L., 2008. Energy dissipation in fracture of bulk metallic glasses via inherent competition between local softening and quasi-cleavage. Philos. Mag. 88, 407–426.

Jin, X., Keer, L.M., Wang, Q., 2011. A closed-form solution for the Eshelby tensor and the elastic field outside an elliptic cylindrical inclusion. J. Appl. Mech. 78.

Johnson, W., Samwer, K., 2005. A universal criterion for plastic yielding of metallic glasses with a (T/T g) 2/3 temperature dependence. Phys. Rev. Lett. 95, 195501.

Ke, H., Zeng, J., Liu, C., Yang, Y., 2014. Structure heterogeneity in metallic glass: modeling and experiment. J. Mater. Sci. Technol. 30, 560–565.

Liu, Y., Wang, D., Nakajima, K., Zhang, W., Hirata, A., Nishi, T., Inoue, A., Chen, M., 2011. Characterization of nanoscale mechanical heterogeneity in a metallic glass by dynamic force microscopy. Phys. Rev. Lett. 106, 125504.

Ma, E., Ding, J., 2016. Tailoring structural inhomogeneities in metallic glasses to enable tensile ductility at room temperature. Mater. Today 19, 568–579.

Maloney, C.E., Lemaitre, A., 2006. Amorphous systems in athermal, quasistatic shear. Phys. Rev. E 74, 016118.

Mayr, S., 2009. Relaxation kinetics and mechanical stability of metallic glasses and supercooled melts. Phys. Rev. B 79, 060201.

Meng, C., Heltsley, W., Pollard, D.D., 2012. Evaluation of the Eshelby solution for the ellipsoidal inclusion and heterogeneity. Comput. Geosci. 40, 40–48.

Miracle, D.B., 2004. A structural model for metallic glasses. Nat. Mater. 3, 697–702.

Mura, T., 2013. Micromechanics of Defects in Solids. Springer Science & Business Media.

Nomoto, K., Ceguerra, A.V., Gammer, C., Li, B., Bilal, H., Hohenwarter, A., Gludovatz, B., Eckert, J., Ringer, S.P., Kruzic, J.J., 2021. Medium-range order dictates local hardness in bulk metallic glasses. Mater. Today 44, 48–57.

Pan, D., Inoue, A., Sakurai, T., Chen, M., 2008. Experimental characterization of shear transformation zones for plastic flow of bulk metallic glasses. Proc. Natl. Acad. Sci. 105, 14769–14772.

Petch, N., 1953. The cleavage strength of polycrystals. J. Iron Steel Inst. 174, 25–28.

Ross, P., Küchemann, S., Derlet, P.M., Yu, H., Arnold, W., Liaw, P., Samwer, K., Maaß, R., 2017. Linking macroscopic rejuvenation to nano-elastic fluctuations in a metallic glass. Acta Mater. 138, 111–118.

Schuh, C.A., Hufnagel, T.C., Ramamurty, U., 2007. Mechanical behavior of amorphous alloys. Acta Mater. 55, 4067–4109.

Song, K., Han, X., Pauly, S., Qin, Y., Kosiba, K., Peng, C.X., Gong, J., Chen, P., Wang, L., Sarac, B., 2018a. Rapid and partial crystallization to design ductile CuZr-based bulk metallic glass composites. Mater. Des. 139, 132–140.

Song, W., Meng, X., Wu, Y., Cao, D., Wang, H., Liu, X., Wang, X., Lu, Z., 2018b. Improving plasticity of the Zr46Cu46Al8 bulk metallic glass via thermal rejuvenation. Sci. Bull. 63, 840–844.

Şopu, D., Moitzi, F., Mousseau, N., Eckert, J., 2020a. An atomic-level perspective of shear band formation and interaction in monolithic metallic glasses. Appl. Mater. Today 21, 100828.

Şopu, D., Scudino, S., Bian, X., Gammer, C., Eckert, 2020b. Atomic-scale origin of shear band multiplication in heterogeneous metallic glasses. Scr. Mater. 178, 57–61.

Şopu, D., Stukowski, A., Stoica, M., Scudino, S., 2017. Atomic-level processes of shear band nucleation in metallic glasses. Phys. Rev. Lett. 119, 195503.

Sun, B., Song, K., Pauly, S., Gargarella, P., Yi, J., Wang, G., Liu, C., Eckert, J., Yang, Y., 2016. Transformation-mediated plasticity in CuZr based metallic glass composites: a quantitative mechanistic understanding. Int. J. Plast. 85, 34–51.

Tao, K., Li, F., Liu, Y., Pineda, E., Song, K., Qiao, J., 2022. Unraveling the microstructural heterogeneity and plasticity of Zr50Cu40Al10 bulk metallic glass by nanoindentation. Int. J. Plast. 154, 103305.

Wakeda, M., Shibutani, Y., 2010. Icosahedral clustering with medium-range order and local elastic properties of amorphous metals. Acta Mater. 58, 3963–3969.

Wang, N., Ding, J., Luo, P., Liu, Y., Li, L., Yan, F., 2018a. Chemical variation induced nanoscale spatial heterogeneity in metallic glasses. Mater. Res. Lett. 6, 655–661.

Wang, N., Ding, J., Yan, F., Asta, M., Ritchie, R.O., Li, L., 2018b. Spatial correlation of elastic heterogeneity tunes the deformation behavior of metallic glasses. NPJ Comput. Mater. 4, 1–10.

Wang, Q., Ding, J., Zhang, L., Podryabinkin, E., Shapeev, A., Ma, E., 2020. Predicting the propensity for thermally activated β events in metallic glasses via interpretable machine learning. NPJ Comput. Mater. 6, 1–12.

Wang, T., Hou, Q., Zhang, L., 2022. Enhanced heterogeneity and plasticity in a Zr-Cu–Al bulk metallic glass with micro-addition of oxygen. Mater. Sci. Eng. A 831, 142222.

Wang, W.H., Dong, C., Shek, C., 2004. Bulk metallic glasses. Mater. Sci. Eng. R Rep. 44, 45–89.

Xu, D., Lohwongwatana, B., Duan, G., Johnson, W.L., Garland, C., 2004. Bulk metallic glass formation in binary Cu-rich alloy series–Cu100− xZrx (x= 34, 36, 38.2, 40 at.%) and mechanical properties of bulk Cu64Zr36 glass. Acta Mater. 52, 2621–2624.

Yang, Y., Zeng, J., Volland, A., Blandin, J., Gravier, S., Liu, C.T., 2012. Fractal growth of the dense-packing phase in annealed metallic glass imaged by high-resolution atomic force microscopy. Acta Mater. 60, 5260–5272.

Yuan, S., Branicio, P.S., 2020. Gradient microstructure induced shear band constraint, delocalization, and delayed failure in CuZr nanoglasses. Int. J. Plast. 134, 102845.

Zhang, L., Wang, Y., Pineda, E., Yang, Y., Qiao, J., 2022a. Achieving structural rejuvenation in metallic glass by modulating β relaxation intensity via easy-to-operate mechanical cycling. Int. J. Plast. 157, 103402.

Zhang, Z., Ding, J., Ma, E., 2022b. Shear transformations in metallic glasses without excessive and predefinable defects. Proc. Natl. Acad. Sci. 119, e2213941119.

Zhao, L., Han, D., Guan, S., Lu, X., Chan, K., Wang, G., 2021. Simultaneous improvement of plasticity and strength of metallic glasses by tailoring residual stress: role of stress gradient on shear banding. Mater. Des. 197, 109246.

Zhao, P., Li, J., Hwang, J., Wang, Y., 2017. Influence of nanoscale structural heterogeneity on shear banding in metallic glasses. Acta Mater. 134, 104–115.

Zhao, P., Li, J., Wang, Y., 2013. Heterogeneously randomized STZ model of metallic glasses: softening and extreme value statistics during deformation. Int. J. Plast. 40, 1–22.

Zhao, P., Li, J., Wang, Y., 2014. Extended defects, ideal strength and actual strengths of finite-sized metallic glasses. Acta Mater. 73, 149–166.

Zhou, Q., Du, Y., Han, W., Ren, Y., Zhai, H., Wang, H., 2019. Identifying the origin of strain rate sensitivity in a high entropy bulk metallic glass. Scr. Mater. 164, 121–125.

Zhu, F., Song, S., Reddy, K.M., Hirata, A., Chen, M., 2018. Spatial heterogeneity as the structure feature for structure–property relationship of metallic glasses. Nat. Commun. 9, 3965.

Zink, M., Samwer, K., Johnson, W., Mayr, S., 2006. Plastic deformation of metallic glasses: size of shear transformation zones from molecular dynamics simulations. Phys. Rev. B 73, 172203.

Kalogirou, S., 2016. Spatial Analysis. http://hdl.handle.net/11419/5029.